



Publication Year	2020
Acceptance in OA@INAF	2022-03-16T15:09:34Z
Title	Unveiling pure-metal ejecta X-ray emission in supernova remnants through their radiative recombination continuum
Authors	pŷ G R E C O , E M A N U E L E ; V i n k , J a c c o ; M i c e l i , M a r c o ; O R L A Vladimir; et al.
DOI	10.1051/0004-6361/202038092
Handle	http://hdl.handle.net/20.500.12386/31620
Journal	ASTRONOMY & ASTROPHYSICS
Number	638

Unveiling pure-metal ejecta X-ray emission in supernova remnants through their radiative recombination continuum

Emanuele Greco^{1,2,3}, Jacco Vink^{3,4,5}, Marco Miceli^{1,2}, Salvatore Orlando², Vladimir Domček^{3,4}, Ping Zhou³, Fabrizio Bocchino², and Giovanni Peres^{1,2}

¹ Dipartimento di Fisica e Chimica, Università degli Studi di Palermo, Piazza del Parlamento 1, 90134 Palermo, Italy

² INAF – Osservatorio Astronomico di Palermo, Piazza del Parlamento 1, 90134, Palermo Italy
e-mail: emanuele.greco@inaf.it

³ Anton Pannekoek Institute for Astronomy, University of Amsterdam, Science Park 904, 1098 XH Amsterdam, The Netherlands

⁴ GRAPPA, University of Amsterdam, Science Park 904, 1098 XH Amsterdam, The Netherlands

⁵ SRON, Netherlands Institute for Space Research, Utrecht, The Netherlands

Received 3 April 2020 / Accepted 26 April 2020

ABSTRACT

Context. Spectral analysis of X-ray emission from ejecta in supernova remnants (SNRs) is hampered by the low spectral resolution of CCD detectors, which typically creates a degeneracy between the best-fit values of chemical abundances and the plasma emission measure. The combined contribution of shocked ambient medium and ejecta to the emerging X-ray emission further complicates the determination of the ejecta mass and chemical composition. This degeneracy leads to big uncertainties in mass estimates and can introduce a bias in the comparison between the ejecta chemical composition derived from the observations and the yields predicted by explosive nucleosynthesis models.

Aims. We explore the capabilities of present and future spectral instruments with the aim of identifying a spectral feature that may allow us to discriminate between metal-rich and pure-metal plasmas in X-ray spectra of SNRs.

Methods. We studied the behavior of the most common X-ray emission processes of an optically thin plasma in the high-abundance regime. We investigated spectral features of bremsstrahlung, radiative recombination continua (RRC), and line emission, by exploring a wide range of chemical abundances, plasma temperatures, and ionization parameters. We then synthesized X-ray spectra from a state-of-the-art 3D hydrodynamic simulation of Cas A, by using the response matrix from the *Chandra* ACIS-S charged-coupled device detector and that of the XRISM/Resolve X-ray calorimeter spectrometer.

Results. We found that a bright RRC shows up when the plasma is made of pure-metal ejecta, and a high spectral resolution is needed to actually identify this ejecta signature. We tested and verified the applicability of our novel diagnostic tool and we propose a promising target for the future detection of such spectral feature: the southeastern Fe-rich clump of Cas A.

Conclusions. While there is no way to unambiguously reveal pure-metal ejecta emission with CCD detectors, X-ray calorimeters will be able to pinpoint the presence of pure-metal RRC and to recover correctly absolute mass and the chemical composition of the ejecta, opening a new window on the link between progenitor star, supernova and SNRs.

Key words. ISM: abundances – ISM: supernova remnants – ISM: individual objects: Cas A – X-rays: general – X-rays: individuals: Cas A

1. Introduction

Supernova remnants (SNRs), the outcome of supernova (SN) explosions, are extended sources with a complex morphology that depends on the properties of the progenitor star and of the ambient medium, and on the processes associated with the SN explosion. After the explosion, the ejecta of the progenitor star expand behind the SN blast wave, which interacts with the interstellar medium (ISM) by heating it up to X-ray emitting temperatures. As the forward shock moves outwards, a reverse shock penetrates and heats the cold expanding ejecta to X-ray emitting temperatures, leading to additional X-ray emission.

X-ray spectral analysis of SNRs is a powerful tool to study the chemical composition and mass of the shocked ejecta. Having information on these quantities is fundamental to knowing more about the progenitor star, the SN explosion, and the explosive nucleosynthesis processes. X-ray spectra of SNRs typically also include the contribution of the shocked ISM, thus making it more difficult to disentangle the contributions of the continuum

and line emission from the ejecta and the swept-up gas, and to infer their physical and chemical properties. Moreover, X-ray spectral analysis of SNRs performed with charge-coupled device (CCD) detectors with moderate spectral resolution ($R \sim 5\text{--}100$) is usually affected by a degeneracy between the best-fit values of chemical abundances and the plasma emission measure. In fact, because of the low energy resolution, the blending between different emission lines can create a “false continuum”, which makes it difficult to constrain the real continuum flux, especially below 4 keV. Thus, it is possible to describe a certain spectrum either with high abundances and low emission measure, or vice versa. This degeneracy leads to big uncertainties in the mass estimates and may even hide the existence of pure-metal ejecta plasma in SNRs (Vink et al. 1996).

Such uncertainty can be partially addressed by measuring relative abundances between elements, typically by adopting Si or Fe as a reference (e.g., Willingale et al. 2002; Miceli et al. 2006, 2008; Kumar et al. 2012; Lopez et al. 2014; Frank et al. 2015; Zhou & Vink 2018; Zhou et al. 2019). On the other

hand, this approach does not allow us to unambiguously derive absolute mass estimates for the yields in SNe. The comparison with theoretical nucleosynthesis yields (e.g., Woosley & Weaver 1995; Thielemann et al. 1996; Nomoto et al. 1997; Nakamura et al. 1999; Sukhbold et al. 2016) can only be performed through abundances ratios and may lead to a misunderstanding of the effective explosion mechanism or of the actual progenitor star properties. In order to have a fully reliable estimate of the abundance and of the mass of each element and to correctly compare these values with the theoretical predictions, a tool able to precisely estimate the absolute abundances of ejecta is required.

In this paper, we present a study on the behavior of the main emission processes in SNRs in the high-abundance regime: Bremsstrahlung (free–free process, indicated with FF), radiative recombination continua (free-bound process, RRC or FB) and line emission. We performed a set of spectral simulations in order to identify a signature of pure-metal ejecta emission in the X-ray spectra of SNRs. We identified a novel diagnostic tool and successfully tested its applicability by adopting the Galactic SNR Cassiopeia A (hereafter Cas A) as a benchmark.

The paper is organized as follows: we identify and describe the nature of the pure-metal ejecta signature in Sect. 2; in Sect. 3 we describe the synthesis method and the resulting synthetic spectra; in Sect. 4 we investigate the possible detection of pure-metal ejecta emission in Cas A; in Sect. 5 we discuss our results and summarize our conclusions.

2. X-ray emission of metal-rich plasma

In this section we recall the physics involved in the thermal emission of an optically thin plasma by focusing especially on the high-abundance regime. We show the results of our spectral simulations and the most relevant features related to the X-ray emission of a pure-metal plasma.

2.1. Main X-ray emission processes

The X-ray emitting plasma in SNRs is optically thin and its emission depends on binary collisions between electrons and ions. At a fixed temperature, T , the emissivity is determined by the emission measure (EM), defined as $EM = \int n_e n_H dV$, where n_e is the electron density and n_H is the ion density of hydrogen (H) (for solar abundances, $n_e \approx n_H$). In the following, we briefly recall the emissivity equations for all the emission processes mentioned in Sect. 1.

The emissivity of the line emission for a particular transition $j \rightarrow i$ of an element z is (Mewe 1999)

$$P_{ji} \propto A_z n_H n_e F(T) \text{ photons cm}^{-3} \text{s}^{-1}, \quad (1)$$

where A_z is the abundance of the element z and $F(T)$ is a function indicating the temperature dependence due to the combined effects of ionization and excitation, which sharply peaks at the characteristic line temperature.

The total bremsstrahlung emissivity is given by the sum of the emissivities of all ion species (Eq. (2), Mewe 1999),

$$\varepsilon_{\text{ff}} \propto \sum_i Z_i^2 n_e n_i T^{-1/2} \exp\left(\frac{-h\nu}{kT}\right) \text{ erg cm}^{-3} \text{s}^{-1} \text{Hz}^{-1}, \quad (2)$$

where Z_i and n_i are the effective charge and density of the ion i . In a plasma with solar (or mildly enhanced) abundances, the main contribution to the bremsstrahlung emission originates from H ions and electrons stripped from H atoms, since this element is by far the most abundant (values of the proto-solar

Table 1. Proto-solar abundances, expressed in logarithmic units with $H = 12.0$, by definition, according to Lodders et al. (2009).

Element	Abundance (log units)
H	12
He	10.987
C	8.443
O	8.782
Ne	8.103
Mg	7.599
Si	7.586
S	7.210
Ar	6.553
Ca	6.367
Fe	7.514
Ni	6.276

abundances in logarithmic units according to Lodders et al. 2009 are shown in Table 1). In the pure-metal ejecta (or extremely metal-rich) scenario, instead, we expect the heavy ions and electrons stemming from them to significantly contribute to the FF emission.

Equation (3) shows the emissivity for the FB process (Liedahl 1999):

$$\varepsilon_{\text{fb}} \propto n_e n_{i+1} \left(\frac{h\nu}{kT^{1/2}} \right)^3 \exp\left(\frac{-h\nu + \chi}{kT}\right) \text{ erg cm}^{-3} \text{s}^{-1} \text{Hz}^{-1}, \quad (3)$$

where n_{i+1} is the ion density of the recombining ion, $h\nu$ is the X-ray photon energy, and χ is the ionization energy. The width of the RRC is $\Delta\nu \approx kT$ and if $kT \ll h\nu$ the emission results in relatively narrow, line-like emission peaks near the series limits of lines. If $kT \gg h\nu$ the RRC is wide and looks like a continuum distribution, similar in shape to FF above the RRC edge. Up to now, this contribution has been observed only in recombining (overionized) plasmas like those detected in a large sample of mixed morphology SNRs during the last decade (e.g., Yamaguchi et al. 2009; Matsumura et al. 2017; Greco et al. 2018 for IC443; Ozawa et al. 2009; Miceli et al. 2010 for W49b, Zhou et al. 2011; Uchida et al. 2012 for W44; Sawada & Koyama 2012 for W28).

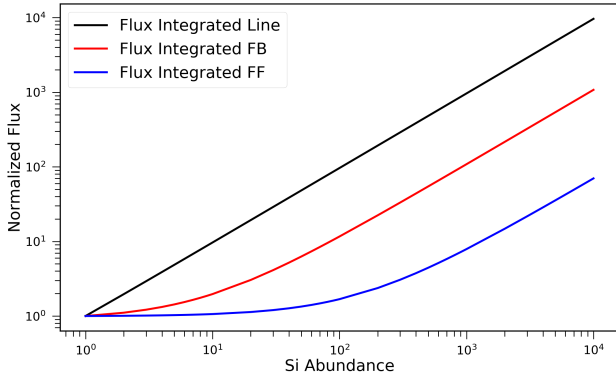
2.2. X-ray spectral signatures of pure-metal ejecta

We performed spectral simulations using the X-ray spectral analysis code SPEX (version 3.04.00 with SPEXACT 2.07.00, Kaastra et al. 1996) with the aim of investigating the behavior of the X-ray emission processes at high abundances. Considering a plasma in collisional ionization equilibrium (CIE), we studied the dependence of the flux on the abundance of two elements: silicon (Si) and iron (Fe). For our simulations, we considered the energy ranges reported in Table 2¹. The SiLine band includes the Si XIII (1.865 keV) and Si XIV (2.006 keV) emission lines, while the SiCont band was chosen to cover the emission at energies slightly above that of the Si XIII recombination edge (2.438 keV) and excluding the Si XIV recombination edge (2.673 keV). The FeLine band includes the forest of Fe L-lines for ions Fe XVII–XXIII, while the FeCont band covers the emission at energies above the Fe XXIV recombination edge (2.023 keV). Values

¹ The S abundance, as well the abundance of all other elements, is fixed to 1. Thus, even if the S XVI line is present at 2.623 keV, it does not affect our results.

Table 2. Energy bands adopted for the X-ray fluxes in Fig. 1.

Band name	Energy range (keV)
SiLine	1.79–2.01
SiCont	2.47–2.67
FeLine	1.2–1.4
FeCont	2.05–2.15

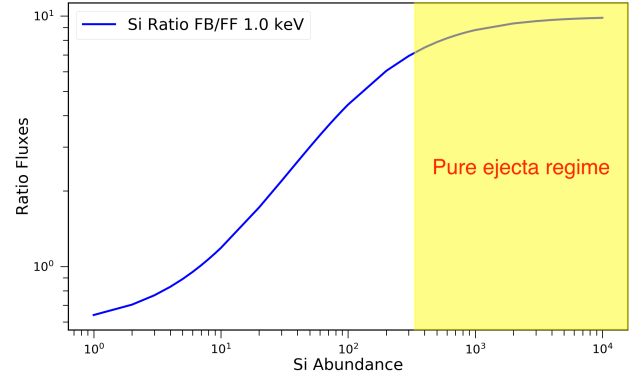
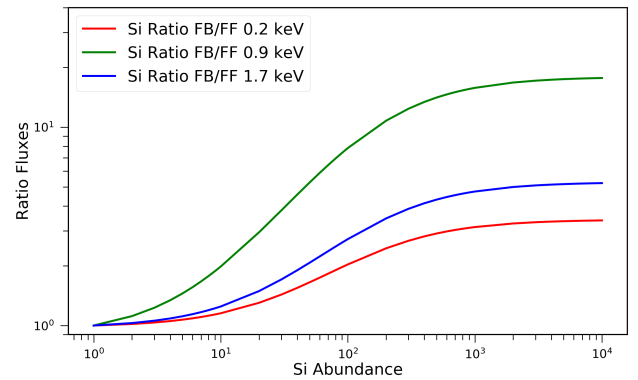

Fig. 1. X-ray fluxes of different emission processes (in the corresponding energy bands, see Table 2) as a function of Si abundance for a plasma temperature of 1 keV. All values are normalized to those obtained for solar abundances.

of the ionization energy are taken from Lide (2003) and the line energies are taken from AtomDB WebGuide².

In the following, we present the results obtained for Si for the sake of clarity, since the Fe emission shows a very complex line pattern up to energies close to those of its RRC. The results obtained for Fe are analogous to those obtained for Si and are described in detail in Appendix A.

Figure 1 shows the integrated flux for each emission process in the corresponding energy band, for a plasma temperature of 1 keV, normalized to that obtained for solar abundances. The flux of line emission increases linearly with the abundance (as predicted by Eq. (1)). The total FB emission shows a weak increase for abundance values between 1 and 10 because the FB emission associated with Si is only a fraction of the total FB emission. Once $A_{\text{Si}} \gtrsim 10$, the total FB emission is due mainly to the Si FB and we observe a linear dependence (as predicted by Eq. (3)). The FF emission is substantially insensitive to the increasing abundance until values of a few hundred are reached; then, it increases with the abundance like the FB and line processes. This is because for abundances $A_{\text{Si}} \lesssim 10^2$, the FF emission produced by electrons originally belonging to H (hereafter H-electrons) overcomes that of electrons stripped from Si (Si-electrons). For solar abundances the number of H-electrons is about 10^4 times the number of Si-electrons (Table 1 and Eq. (2)), therefore, by only slightly increasing the Si abundance, the global contribution to the FF emission is still mainly associated with H-electrons (and H ions).

As abundances on the order of a few hundred are reached, the number of Si-electrons is not negligible with respect to the number of H-electrons. Moreover, in this regime, which we call the pure-metal ejecta regime, the contribution of Si ions to the electron scattering becomes important. For these high abundances, therefore, the term including the Si contribution


Fig. 2. Ratio between the FF and FB fluxes shown in Fig. 1 as a function of the Si abundance for a plasma temperature of 1 keV.

Fig. 3. Same as Fig. 2 for plasma temperatures of 0.2 keV (red line), 0.9 keV (green), and 1.7 keV (blue).

becomes the dominant one in the summation of Eq. (2) (given the dependence on Z_i^2 , with $Z = 12$ for He-like Si) and we thus observe the expected linear increase with the abundance. Figure 2 shows the FB over FF flux ratio: the observed flattening in the flux ratio reflects the pure-metal ejecta regime discussed so far.

We also investigated how the FB to FF flux ratio depends on the plasma temperature. We repeated the simulations described above by exploring temperatures in the range $kT = 0.2$ – 3 keV with a step of 0.1 keV. Figure 3 shows the FB to FF flux ratios for three different temperatures, namely $kT = 0.2$ keV, $kT = 0.9$ keV, and $kT = 1.7$ keV. By increasing the temperature in the range 0.2–0.8 keV, the slope σ of the FB to FF ratio as a function of Si abundance increases; that is, with high plasma temperature, the FB contribution becomes more visible than the FF. However, at $kT \sim 0.9$ keV, σ reaches its maximum and a further increase in temperature leads to lower values of σ . The observed trend at energies below 0.9 keV is due to the increasing degree of Si ionization and the subsequent higher number of free electrons combined with the increasing width of the RRC, which is spread out at higher temperatures thus reducing the effect in the 2.47–2.67 keV band. On the other hand, at energies above this threshold, the electrons are so energetic that they can escape recombination while still increasing the FF emission. The value of the temperature threshold depends on the element considered, because of the different degree of ionization at a given temperature and of the corresponding number of vacancies in the ion itself. Heavier elements have higher thresholds (see Fig. A.1 for the Fe case) also because of the stronger ion electrostatic field. We found that, in the Si case, the FB to FF ratio is maximized

² <http://www.atomdb.org/Webguide/webguide.php>.

Table 3. Main characteristics of ACIS-S (*Chandra*) and Resolve (XRISM) detectors.

Detector technology	ACIS-S CCD	Resolve microcal.
Field of view	9' × 9'	3' × 3'
PSF	0.5''	1.7'
Energy res. at 6 keV (eV)	50	5
Eff. Area at 1 keV (cm ²)	340	160
Eff. Area at 6 keV (cm ²)	230	210
Energy range (keV)	0.15–12	0.3–12

when the electron temperature is in the range $kT = 0.6\text{--}1.2$ keV. In the Fe case, the corresponding range is $kT = 1.5\text{--}3.5$ keV (see Appendix A).

In conclusion, we expect that the spectral signature of pure-metal ejecta must be related to the enhanced FB emission. Therefore, a careful study of edges continua can be adopted as a diagnostic tool to reveal pure-metal ejecta in SNRs.

3. Synthetic X-ray spectra

To investigate the observability of pure-metal ejecta emission in SNRs, we produced synthetic spectra by folding our spectral models with the response matrix of actual detectors. We also included the contribution of the ISM X-ray emission. Pure-metal ejecta can be distributed on large, expanding shells as well as concentrated in dense clumps embedded in an environment of shocked ISM, where the mixing between ISM and ejecta is less remarkable (as Hwang & Laming 2003 found for the Fe cloudlets in Cas A). In any case, the ejecta emission is always superimposed onto the emission stemming from the shocked ISM. In this section, we assume a generic value for the column density equal to $n_H = 5 \times 10^{21} \text{ cm}^{-2}$, unless otherwise stated.

For our simulations, we used the response matrices of ACIS-S³, a CCD detector on board the *Chandra* X-ray telescope⁴ and Resolve, a microcalorimeter that will be on board XRISM⁵, the JAXA/NASA X-ray telescope expected to be launched in 2021. The main instrumental characteristics of these instruments are summarized in Table 3. XRISM will have lower effective area and spatial resolution than *Chandra* but, thanks to the microcalorimeter, its spectral resolution will be better than that of *Chandra* by a factor of ten.

3.1. ACIS-S

Here, we show that CCD detectors are not able to detect the RRC edge. To do that, we simulated a *Chandra* ACIS-S synthetic spectrum (1 Ms of exposure time) of a plasma in CIE with ejecta abundance set to 3 for all the elements except for Si, which is set to 300, and an electron temperature of 0.8 keV (Fig. 4). The Si abundance is so high that the corresponding emission lines dominate the whole spectrum. Even if this scenario is not realistic, because we have not yet included the contribution of the ISM X-ray emission, it allows us to notice that the corresponding spectrum does not show any spectral signatures related to the

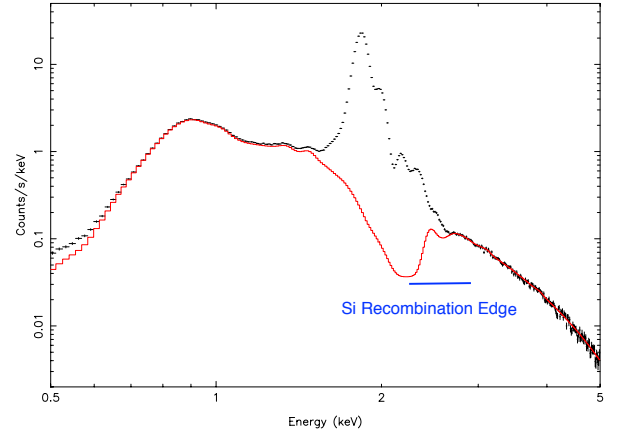


Fig. 4. Synthetic ACIS-S spectra with high Si abundance. Black: synthetic ACIS-S spectrum of a CIE plasma with abundance of all elements set to 3, with the exception of Si abundance set to 300; $kT = 0.8$ keV and $EM = 1.5 \times 10^{55} \text{ cm}^{-3}$. Red solid: same spectrum but with the Si line emission subtracted, but Si contributions to the FF and FB continuum are still included.

RRC emission, which is expected to be present on the basis of the study of the fluxes discussed in the previous section. This is because the poor resolution of the CCD spectrometer makes the He-Si and H-Si lines heavily broadened. The line broadening blurs the recombination edges, thus hiding the spectral signature of pure-metal ejecta emission. In fact, by ignoring only the Si line emission (Si contributions to the FF and FB continuum are still included), the resulting spectrum (in red in Fig. 4) shows, as expected, a prominent edge of recombination at the characteristic energy of Si-RRC.

The difficulty of observing enhanced FB emission and the contamination by shocked ISM hamper the identification of pure-metal ejecta in CCD spectra. As an example, we here show a synthetic SNR spectrum (a more realistic simulation, performed for a specific case, is presented in Sect. 4). We considered a spherical clump of Si-rich ejecta (Si abundance set to 300, as before) with radius $R_{\text{clump}} = 0.5$ pc and temperature $kT_{\text{clump}} = 0.8$ keV, surrounded by a colder ISM with temperature $kT_{\text{ISM}} = 0.15$ keV. If we assume a density particle n_e equal to 3 cm^{-3} and pressure equilibrium between the clump and the ISM, and extract the spectrum from a box corresponding to a region of $8 \text{ pc} \times 8 \text{ pc}$ (in the plane of the sky) and extending 8 pc along the line of sight, the ISM emission measure is four orders of magnitude larger than that of the clump (see Table 4 for details). This case is the one in which the effect is maximized but, as we will also see in Sect. 4, this remains visible in the whole typical temperature range of SNRs and our conclusions do not depend on this choice. We synthesized the ACIS-S X-ray spectrum using the CIE+CIE pure-metal model described in Table 4. We assumed a distance of 1 kpc and an unrealistically high exposure time of 10^8 s in order to highlight the features. In Sect. 4 we will discuss cases with a more realistic exposure time. We adopted the response and ancillary files produced during the data reduction of *Chandra* observation 114 (PI Holt). Figure 5 shows the resulting synthetic ACIS-S spectrum. As a comparison, we also produced a spectrum starting from the mild-ejecta model described in Table 4, namely a model with the same parameters as those of the pure-metal model except only for the Si abundance, which is set to 3 (instead of 300), and for the ejecta EM, set to $1.6 \times 10^{57} \text{ cm}^{-3}$. This new spectrum is shown in Fig. 5. A comparison between the two spectra does not reveal

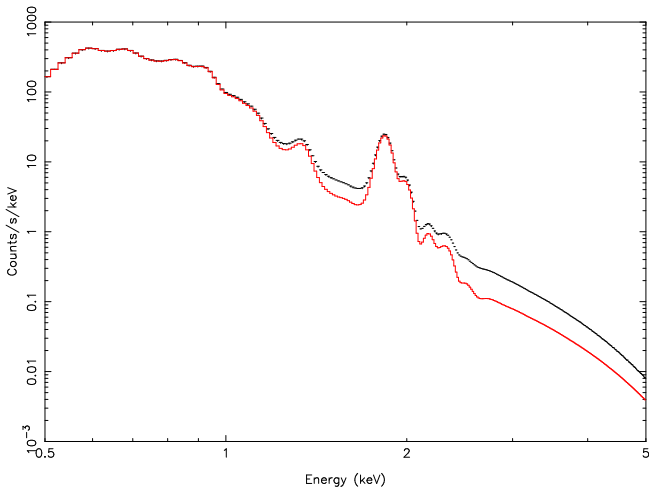
³ Using the *XMM-Newton*/MOS response matrix instead of the *Chandra*/ACIS-S leads to identical results.

⁴ <https://heasarc.gsfc.nasa.gov/docs/chandra/chandra.html>

⁵ <http://xrism.isas.jaxa.jp>

Table 4. Parameters of the ISM (CIE) plus pure-Si (CIE) or mild-Si models used for the spectral synthesis with the corresponding inferred Si and ejecta masses.

Parameter	ISM	Pure-metal	Mild-ejecta
EM (cm^{-3})	1.6×10^{59}	1.5×10^{55}	1.5×10^{57}
kT (keV)	0.15	0.8	0.8
Si Abundance	1	300	3
Si mass (M_{\odot})	/	0.015	0.0016
Ejecta mass (M_{\odot})	/	0.06	0.6

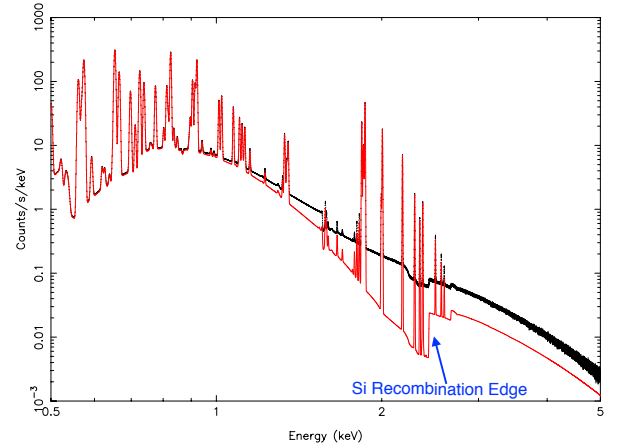
**Fig. 5.** Synthetic ACIS-S spectra of ISM+pure-Si (pure-metal model, red) and ISM+Si-rich (mild-ejecta model, black) plasmas.

any clear difference that could be related to the pure-metal ejecta emission (even with an unrealistically high exposure time of 10^8 s). However, as we can see from the derived masses in Table 4, in the pure-metal ejecta the total mass estimate goes down, but the mass of the considered element, Si in this case, goes up. We have two different models, with two different masses prediction, which are substantially indistinguishable. Spectra in Fig. 5 confirm that the degeneracy between abundance and emission measure is a serious issue, which is intrinsically due to the instrumental characteristics of the CCD cameras and does not depend on the statistics of the observation. The ability to close off and identify the presence of FB contributions offers a unique diagnostic tool to assess whether the spectrum is coming from a highly enriched, but still hydrogen-dominated plasma, or from a pure-metal ejecta plasma.

3.2. Resolve

Here, we further show that the degeneracy between abundance and emission measure is intrinsically due to the instrumental characteristics of the CCD cameras and does not depend on the statistics of the observation. We repeated the spectral simulations discussed above by folding the pure-metal model and the mild-ejecta model with the Resolve response matrix⁶.

Figure 6 shows the pure-metal case and the mild-ejecta case, again assuming an exposure time of 10^8 s. Thanks to the high

**Fig. 6.** Same as Fig. 5 but the model is folded through the Resolve response matrix.

spectral resolution of the microcalorimeter, it is now possible to observe a clear spectral difference between the two scenarios. As expected on the basis of the study presented in Sect. 2, a bright edge of recombination shows up at ~ 2.5 keV (i.e., the He-Si RRC typical energy) when the abundance of Si is 300. Figure 6 also clearly shows that the recombination edge and the RRC are much dimmer in the mild-ejecta case. We stress that, in the pure-metal ejecta regime, even if the bremsstrahlung emission from the shocked ISM enhances the continuum emission and strongly reduces the equivalent width of emission lines, the RRC still emerges above the FF emission at energies > 2.5 keV. Therefore, according to our simulations, the enhanced FB emission is a better tracer of pure-metal ejecta than the line equivalent width.

High resolution spectrometers like Resolve (and, in the future, X-IFU on board the Advanced Telescope for High-Energy Astrophysics, ATHENA) are therefore capable of pinpointing the enhancement in the FB emission associated with a plasma with extremely high metallicity.

4. Pure-metal ejecta in Cas A

The simulations described above show that the enhancement in the RRC emission can be a strong signature of pure-metal ejecta and that such a spectral signature can be detected with high resolution spectrometers, while being almost impossible to be observed with CCD detectors. We here apply our diagnostic tool to a real case, by focusing on Cas A. In particular, we aim to understand whether it will be possible to pinpoint pure-metal ejecta emission with the Resolve spectrometer.

Cas A is one of the brightest and most studied SNR. It is a young (330 yr old, Thorstensen et al. 2001) SN IIB-type remnant (Krause et al. 2008) at a distance of 3.4 kpc (Reed et al. 1995), which shows many asymmetries and an overall clumpiness (Reed et al. 1995; Hwang & Laming 2003, 2012; Vink & Laming 2003; Hwang et al. 2004; DeLaney et al. 2010; Milisavljevic & Fesen 2013; Lee et al. 2014). In particular, Hwang & Laming (2012) performed a detailed survey of the ejecta distribution in Cas A highlighting the presence of three large-scale Fe-rich clumps. They also confirmed the existence of an Fe-rich cloudlet, previously detected by Hughes et al. (2000) and Hwang & Laming (2003), located within the southeastern clump. In this cloudlet the relative Fe/Si abundance is ~ 20 , while Fe/Si is ~ 5 in the other Fe-rich regions of Cas A.

⁶ Resolve response and ancillary files used are xarm_res_h5ev_20170818.rmf and xarm_res_ft_fa_20170818.arf, available on <https://heasarc.gsfc.nasa.gov/docs/xrism/proposals/>

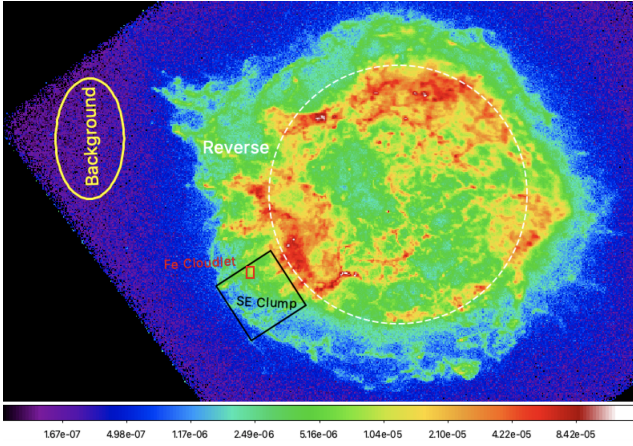


Fig. 7. *Chandra* count-rate image of Cas A in the 0.3–7 keV energy band with a logarithmic color scale. The small red box marks the Fe-rich cloudlet, the black box indicates the region selected in the southeastern Fe-rich clump, the yellow ellipse shows the region chosen for the background, and the dashed white circle marks the nominal position of the reverse shock.

Here, we take advantage of the 3D hydrodynamic (HD) simulation of Cas A performed by [Orlando et al. \(2016; hereafter O16\)](#). This state-of-the-art simulation models the evolution of Cas A from the immediate aftermath of the supernova to the 3D interaction of the remnant with the ambient environment. In particular, we adopted the model configuration that best describes the observed ejecta distribution (run CAS-15MS-1ETA in O16). This model reproduces the observed average expansion rate of the remnant and the shock velocities, and constrains the post-explosion anisotropies responsible for the observed structure and chemical distribution of ejecta. The model can reproduce very well the shocked Fe distribution (both on large and relatively small spatial scales) while the Si (and S) mass seem to be slightly underestimated. We therefore focused on the Fe emission and adopted the HD simulation as a reference template to synthesize the expected X-ray emission. We point out that the remnant evolution modeled by O16 clearly shows that large regions of Cas A are expected to be filled with pure Fe-rich ejecta.

We consistently produced synthetic *Chandra*/ACIS and XRISM/Resolve spectra of the southeastern Fe-rich clump in Cas A from the 3D HD simulation. We compared the synthetic spectra with that observed by *Chandra* and made predictions for the future Resolve observations.

4.1. Data analysis

We analyzed the *Chandra* observation with ID 114 (PI Holt), performed on 30/01/2000. We used the tool *fluximage* to produce a count-rate image of Cas A with a bin size of 1". Figure 7 shows the count-rate image in the 0.3–7 keV energy band together with the regions selected for the spectral extraction. Within the southeastern Fe-rich clump, non-thermal emission from the Cas A reverse shock has been detected ([Gotthelf et al. 2001](#)) and mapped accurately ([Helder & Vink 2008](#)). Since synchrotron X-ray emission is not taken into account in our spectral synthesis code, we carefully selected the large box in the southeastern part of the shell by excluding the reverse shock.

By fitting the cloudlet spectrum we found the same best-fit parameters as [Hwang & Laming \(2003\)](#), including an Fe/Si abundance ratio equal to ~ 20 . In addition, we found that the absolute Fe abundance is not well constrained. In fact, two

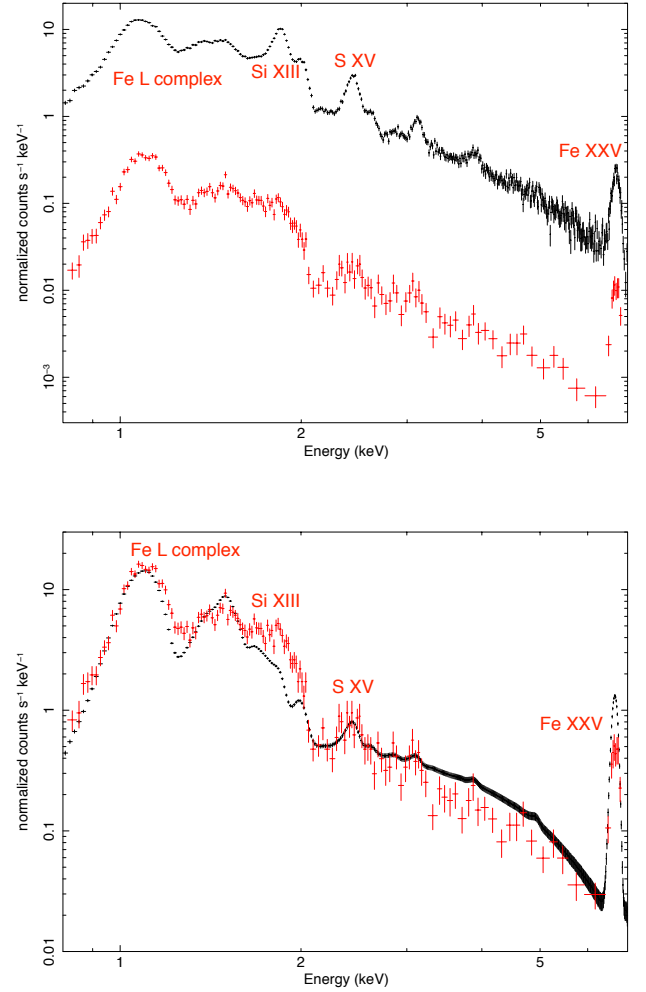


Fig. 8. Comparison between actual *Chandra* spectra. *Upper panel:* *Chandra* ACIS-S spectra extracted from the southeastern Fe-rich clump (black box in Fig. 7) and from the Fe-rich cloudlet (red box in Fig. 7) shown by black and red crosses, respectively. *Lower panel:* *Chandra* ACIS-S synthetic spectrum clump derived from the HD simulation of the southeastern Fe-rich (black crosses). Red crosses show the renormalized observed spectrum of the Fe-rich cloudlet shown in the upper panel for easy comparison with the synthetic spectrum.

statistically equivalent fits with $\chi^2_{\text{red}} = 1.55$ (136 d.o.f.) can be obtained with $A_{\text{Fe}} = 29$ (and $\text{EM} = 1.4 \times 10^{55} \text{ cm}^{-3}$ for the ejecta component) and $A_{\text{Fe}} = 290$ ($\text{EM} = 1.6 \times 10^{54} \text{ cm}^{-3}$). The cloudlet spectrum is shown in the upper panel of Fig. 8⁷: the wide and bright structure at energies ~ 1 keV, reveals the presence of a remarkable complex of Fe L lines, but we do not see any Fe RRC. As explained in Sect. 3, the absence of this feature can be related to the instrumental characteristics of *Chandra*. The upper panel of Fig. 8 also shows the spectrum extracted from the black box of Fig. 7, which presents a very strong Fe emission line complex, but with the addition of bright Si and S emission lines (the Fe/Si abundance ratio is lower than that in the Fe-rich cloudlet, being only ~ 5). This suggests the presence of both Fe-rich and Si-rich ejecta though we cannot exclude that the observed silicon emission may be somehow enhanced by the dust scattering in this region.

⁷ Plots in Fig. 8 are obtained through the spectral analysis software XSPEC ([Arnaud 1996](#)).

4.2. Self-consistent X-ray synthesis tool

We developed a tool to self-consistently synthesize the thermal X-ray emission from the 3D HD simulation. In each cell of the computational domain we derive the local value of temperature, electron density, ionization parameter (τ , defined as the time integral of the electron density computed from the impact with the shock front), total mass, and mass tracer of each element (see O16 for the list of isotopes included in the simulation). The mass tracer describes the mass of a given species as a fraction of the total mass in the cell. Our tool extracts all the aforementioned quantities for each cell and we use these values as input parameters for the non-equilibrium of the ionization optically thin plasma model *neij* (Kaastra & Jansen 1993) based on the atomic database SPEXACT 2.07.00, within SPEX. In particular, for each atomic species i , we derive the local value of ion and electron density and synthesize the corresponding “pure- i ” spectrum in each computational cell. The latter step is done by setting the abundance of all elements except i equal to 0, while i abundance is set to 1. We then sum the resulting spectra over all the species by weighting each term for the corresponding emission measure. Finally, we sum the spectra of all the computational cells within a given region of the domain to derive the global spectrum of a selected area in the numerical simulation. All the spectra are filtered through photoelectric absorption by the interstellar medium, with the appropriate column density (for this region $n_H = 1.5 \times 10^{22} \text{ cm}^{-2}$, Hwang & Laming 2012) and are estimated assuming a distance of 3.4 kpc (Reed et al. 1995). Each spectrum can be folded through the instrumental response matrix (i.e., *Chandra*/ACIS-S or XRISM/Resolve). All the spectra are binned using the optimal bin tool present in SPEX (Kaastra et al. 1996). By selecting the ACIS-S response matrix, we can directly compare the synthetic spectra with those observed, which is crucial for a fine-tuning of the selection of the region for the synthesis.

4.3. Synthesis of Cas A spectra

We selected a region in the southeastern Fe-rich clump with the same size as the black box chosen from the actual *Chandra* data and displayed in Fig. 7 (the spatial resolution of XRISM is not good enough to resolve the Fe-rich cloudlet marked in red in Fig. 7). The resulting synthetic *Chandra* ACIS-S spectrum, obtained assuming an exposure time of 1 Ms, is shown in the lower panel of Fig. 8. The spectrum clearly shows signatures of bright Fe line emission, broadly similar to those actually observed in the corresponding region. At odds with the observations, the synthetic spectrum does not show very bright emission lines from Si and S ions, thus indicating that intermediate mass elements are somehow under-represented in the simulation in this particular region. We point out that we are not aiming to find a perfect agreement between synthetic and observed spectra, but we are interested in providing reliable and robust predictions on the X-ray emission from Fe-rich ejecta. We show below that the lack of bright Si and S emission lines in the synthetic spectra does not affect our conclusions. We here notice that the synthetic spectrum is a good proxy of the real Fe-rich ejecta emission, given that it is extremely similar to the actual spectrum of the Fe-rich cloudlet (red box in Fig. 7). This is shown in Fig. 8, where the observed and renormalized spectra of the cloudlet can be compared with that derived from the HD simulation. We only note some discrepancies in the brightness of the Fe XXV emission line, which is slightly overestimated in the synthetic spectrum. This is due to the fact that, in this region,

the simulated temperature is slightly ($\sim 30\%$) higher than that observed. However, this excess does not affect our conclusions since both actual and modeled temperatures lie in the range in which the Fe FB to FF ratio is maximized (see Appendix A). We only expect a slightly narrower edge of Fe RRC in the actual spectra with respect to that derived from the simulation.

As in the actual data, we found that it is not possible to constrain the Fe abundance in the ACIS-S spectrum of this region. In fact, two statistically equivalent fits that have $\chi^2_{\text{red}} = 1.06$ (138 d.o.f.) can be obtained with $A_{\text{Fe}} = 45$ (and $\text{EM} = 1.3 \times 10^{57} \text{ cm}^{-3}$ for the ejecta component) and $A_{\text{Fe}} = 1200$ ($\text{EM} = 6 \times 10^{55} \text{ cm}^{-3}$). The corresponding Fe mass is therefore highly uncertain, spanning from $M_{\text{Fe}} = 2 \times 10^{-4} M_{\odot}$ to $M_{\text{Fe}} = 4 \times 10^{-3} M_{\odot}$.

We then synthesized the XRISM/Resolve spectrum from the same region, by assuming an exposure time of 1 Ms. The resulting spectrum is shown in Fig. 9. The microcalorimeter spectrometer provides a superior spectral resolution, allowing us to clearly identify all the emission lines and spectral features. We here show that, by analyzing the Resolve synthetic spectrum, it is possible to unambiguously identify the enhanced RRC emission from the recombination of Fe ions, thus revealing the presence of pure-metal ejecta (as predicted in Sect. 3).

We fitted the spectrum with two isothermal components of an optically thin plasma in non-equilibrium of ionization associated with the shocked ISM and ejecta, respectively (hereafter NEI+NEI model). We considered two different scenarios: mild-ejecta and pure-metal ejecta. In the first case, we kept the Fe abundance fixed to ten in the ejecta component (the spectrum with the best-fit model and residuals is shown in the upper panel of Fig. 9); in the second case we left the Fe abundance of the ejecta component free to vary (mid panel of Fig. 9). Best-fit parameters are shown in Table 5.

The spectral residuals and χ^2 show that an Fe abundance > 100 is necessary to properly fit the Fe RRC. The mild-ejecta scenario leads to strong residuals at the recombination edge energy and to a global misrepresentation of the spectrum. As already mentioned in Sect. 3.1, we expect that in the pure-metal ejecta scenario the total mass estimate goes down, but the mass of the considered element, Fe in this case, goes up. Indeed, by fitting the spectrum synthesized with XRISM, we obtained $M_{\text{Fe}} = 4.8^{+0.5}_{-0.4} \times 10^{-3} M_{\odot}$, in good agreement with the value used in the simulation, $4.6 \times 10^{-3} M_{\odot}$. The high spectral resolution provided by the microcalorimeters allows us to reveal the enhanced RRC emission of pure-metal ejecta and this clearly removes the degeneracy between abundance and emission measure in the fitting procedure, leading to a correct estimate of the absolute Fe mass in this area.

As explained above, the HD simulation provides an accurate description of the actual distribution of Fe-rich ejecta in Cas A and is able to reproduce the spectral features observed with *Chandra*. However, the moderate spectral resolution of *Chandra* (and CCD detectors in general) does not allow us to confirm that pure-metal ejecta are present in Cas A, as predicted by the O16 model. If pure-Fe ejecta are actually present in the southeastern limb of Cas A, we expect to pinpoint their presence with XRISM and to correctly derive their mass (see Sect. 5).

As explained above, we expect that the actual spectrum will show more Si and S line emission than that predicted by our simulation (see Fig. 8). Therefore, we should observe brighter Si and S lines and a bright RRC from Si (at energies $E > 2.5 \text{ keV}$, see Fig. 6) and S ($E > 3 \text{ keV}$). These features will not mask out the Fe RRC, thus not affecting our conclusions. In fact, the Si and S lines will be well resolved by the XRISM spectrometer without

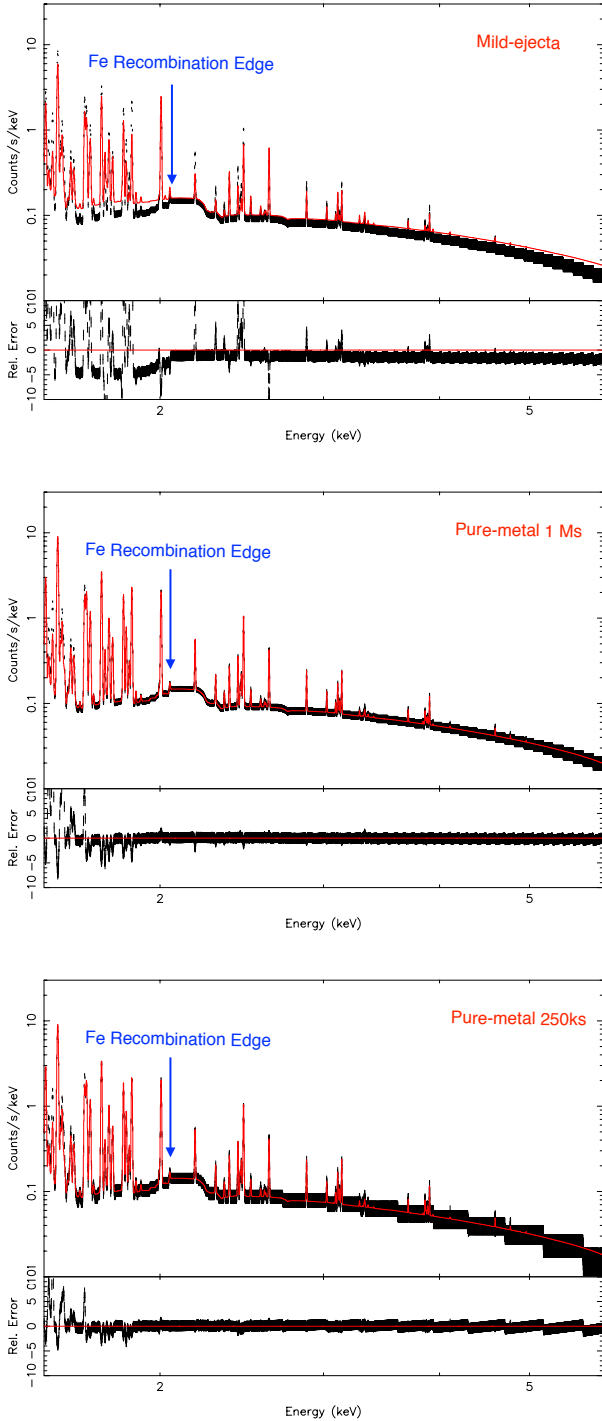


Fig. 9. Synthetic XRISM spectra of the Fe-rich southeastern clump with the corresponding best-fit models and residuals obtained for the mild-ejecta case (*upper panel*), the pure-metal ejecta case (*middle panel*), and the pure-metal ejecta case with an exposure time of 250 ks (*lower panel*). Table 5 provides details of the best-fit parameters.

contaminating the Fe RRC and the Si (and S) RRC; also, edges show up at energies higher than the Fe XXIV recombination energy (2.023 keV).

We note that the residuals at low energy in the lower panel of Fig. 9 are due to our simplified spectral model that includes only one isothermal component for the ejecta. Indeed, our HD simulation shows a relatively broad distribution of plasma temperatures and ionization parameters in the region selected, but

we are fitting the spectrum with only two temperatures and ionization parameters. A multi-component model provides a much better fit to the emission line complexes, but this is beyond the scope of this paper. In any case, even with this more complex spectral model, we verified that an Fe abundance >100 is always required to fit the spectrum.

So far, we have shown the synthetic spectra produced assuming an exposure time of 1 Ms. We are aware that it may not be possible to observe this region of Cas A for such a large amount of time. Therefore, we synthesized the same spectrum as in the upper panel of Fig. 9 assuming an exposure time of 250 ks (lower panel in Fig. 9). The enhanced Fe RRC remains visible in the spectrum and the pure-metal ejecta model describes the spectrum significantly better than the mild-ejecta model. An exposure time shorter than 250 ks may not be sufficient to unambiguously detect the pure-metal ejecta.

5. Discussion and conclusions

In this paper we have shown that spectral analysis carried out with current X-ray detectors suffers from an intrinsic degeneracy in measuring the abundances using line-dominated spectra from SNRs. We studied the behavior of the X-ray emission processes at high abundances, identifying the enhanced RRC as the spectral signature of pure-metal ejecta. We showed that the low energy resolution of current CCD detectors hampers our understanding of the spectra, hiding the characteristic RRC. We found that future microcalorimeter spectrometers, such as Resolve, which will be onboard the XRISM telescope, can address this issue. We also presented a very promising case for the detection of pure-Fe emission in the southeastern clump of Cas A, by using both *Chandra* data and a 3D HD simulation to derive quantitative predictions of the expected Resolve spectrum. The resulting synthetic spectra show bright Fe RRC at an energy of around 2 keV and the fits performed on such spectra can definitely pinpoint the presence, if any, of pure-metal ejecta.

5.1. Implications for SNRs with overionized ejecta components

The RRC features discussed here have a different physical origin with respect to those associated with overionized plasmas that have been detected so far in spectra of mixed-morphology SNR, namely those remnants that show bright radio emission in the outer shells and peaked X-ray emission in the internal ones. When a plasma in equilibrium of ionization undergoes a rapid cooling, the electron temperature is drastically lowered and the plasma degree of ionization is higher than that expected in CIE for the observed electron temperature. In this scenario, the plasma is in a phase of strong recombination and the characteristic spectra show very bright recombination edges. The physical mechanism that causes the rapid cooling of the plasma is still debated and both thermal conduction with nearby molecular clouds (e.g., Okon et al. 2020) and adiabatic expansion (e.g., Zhou et al. 2011, Yamaguchi et al. 2009) have been proposed as viable cooling processes (even for the same object, see Matsumura et al. 2017 and Greco et al. 2018 for IC 443). We verified that the enhanced recombination features related to pure-metal ejecta can be distinguished from those associated with overionization. The upper panel of Fig. 10 shows the continuum emission of an overionized plasma with $\tau_{\text{rec}} = 10^{11} \text{ s cm}^{-3}$, cooled down to $kT_{\text{fin}} = 0.5 \text{ keV}$ from an initial temperature $kT_0 = 5 \text{ keV}$ (typical values for overionized plasmas in SNRs, Matsumura et al. 2017; Greco et al. 2018), and the continuum

Table 5. Best-fit values for the fitting of the synthetic XRISM/Resolve spectrum of the Cas A southeastern region by adopting two thermal components, in the mild-ejecta and pure-metal ejecta scenarios.

Parameter	NEI+NEI (mild-ejecta)	NEI+NEI (pure-metal ejecta)	NEI+NEI (pure-metal ejecta) 250ks
n_H (10^{22} cm^{-2})	1.5 (frozen)		
kT (keV)	$0.5^{+0.3}_{-0.001}$	1.96 ± 0.05	$1.62^{+0.11}_{-0.06}$
τ ($10^{11} \text{ s cm}^{-3}$)	$1.10^{+0.08}_{-0.05}$	1.13 ± 0.04	$1.8^{+0.3}_{-0.2}$
EM (10^{58} cm^{-3})	$0.19^{+0.002}_{-0.17}$	0.150 ± 0.004	$0.20^{+0.02}_{-0.01}$
kT (keV)	$3.9^{+0.3}_{-0.15}$	2.90 ± 0.01	2.89 ± 0.03
τ ($10^{11} \text{ s cm}^{-3}$)	$1.53^{+0.05}_{-0.08}$	2.51 ± 0.02	$2.51^{+0.05}_{-0.03}$
EM (10^{58} cm^{-3})	$0.34^{+0.04}_{-0.001}$	0.056 ± 0.005	$0.002^{+0.0003}_{-0.001}$
Si	$0.415^{+0.003}_{-0.011}$	0.77 ± 0.08	1 ± 1
S	$0.377^{+0.005}_{-0.013}$	$0.93^{+0.08}_{-0.07}$	$2.0^{+2}_{-0.2}$
Ar	0.25 ± 0.02	0.4 ± 0.2	1^{+15}_{-1}
Ca	$0.15^{+0.02}_{-0.03}$	0.49 ± 0.2	1^{+7}_{-1}
Fe	10 (frozen)	119^{+11}_{-9}	300^{+400}_{-100}
χ^2_{red} (d.o.f.)	11.85 (5005)	2.11 (5004)	0.65 (4709)
Counts	1.4×10^6		3.5×10^5

Notes. The abundances of the first component (associated with the ISM) are all frozen to 1. The rightmost column displays the best-fit values obtained from the 250 ks spectrum.

emission of ejecta in the pure-Si regime (Si abundance set to 300). The RRC produced by the overionized plasma is much stronger than that of pure-metal ejecta. This is because in the pure-metal ejecta regime the ratio FB/FF does not increase arbitrarily with the abundance, but reaches a saturation value (see Fig. 2), which is smaller than that obtained for the case of overionization. Moreover, in the case of overionization, the Si-edge is actually composed of two different edges: the one at lower energy is related to the He-like Si, while the second edge, which is the brightest, is associated with H-like Si. This is a characteristic feature of overionized plasmas, since the high degree of ionization leads to an increase in the H-like ions at the expense of the He-like ions. Therefore, both the shape and the intensity of the RRC and edges make it possible to discriminate between pure-metal ejecta and overionized plasmas.

Nevertheless, the case of a pure-metal ejecta overionized plasma also needs to be considered. This scenario may be realistic for the Galactic SNR W49B (Ozawa et al. 2009; Miceli et al. 2010; Zhou et al. 2011; Lopez et al. 2013; Zhou & Vink 2018). The combination of the two effects (pure-metal plasma and overionization) further increases the contribution of the RRC emission and needs to be taken into account to correctly estimate the ionization parameter. The line emission has a crucial role in this scenario. In the lower panel of Fig. 10, we show the same synthetic XRISM spectra displayed in the upper panel of Fig. 10 assuming an exposure time of 100 ks and also including line emission. Even with this realistic exposure time we can easily distinguish the different shapes of the RRCs and discriminate between pure-metal ejecta and overionized plasma. Moreover, the line emission is completely different in the two spectra. In the recombining scenario the Si H-like lines dominate the spectrum and the He-like ones are significantly fainter. At the same time, the overall brightness of Si lines is higher in the pure-metal

scenario, as we expect because of the high abundance. In conclusion, a careful analysis of the line emission is needed to correctly distinguish between the pure-metal ejecta and the recombining scenarios.

5.2. Recovering the absolute mass thanks to RRC with Resolve spectra

The capability of detecting pure-metal ejecta emission is crucial to recover the correct mass of the atomic species in the ejecta. We here show that from the synthetic XRISM spectrum of Cas A (discussed in the previous section) it is possible to properly derive the Fe mass. We compared the Fe mass calculated from the best-fit models of the synthetic XRISM and *Chandra* spectra with the correct value, known from the HD simulation. In order to estimate the filling factor of ejecta and ISM from the analysis of the synthetic spectra, we followed the recipe by Bocchino et al. (1999) under the assumption of pressure equilibrium. As explained in Sect. 4.3, by fitting the *Chandra* synthetic spectrum, we found that the Fe abundance can vary from a few tens to more than 10^3 . By fitting the spectrum synthesized with XRISM, we instead obtained $M_{\text{Fe}} = 4.8^{+0.5}_{-0.4} \times 10^{-3} M_{\odot}$. From the simulation, we know that the correct value of the Fe mass in the region is $4.6 \times 10^{-3} M_{\odot}$. Despite the lower statistics, by fitting the 250 ks XRISM spectrum we obtain $M_{\text{Fe}} = 6^{+5}_{-2} \times 10^{-3}$, which is consistent with the correct value. We stress that an exposure time shorter than 250 ks could lead to an ambiguous detection of the pure-metal ejecta feature. By analyzing the XRISM spectra, we remarkably recover the real mass of the Fe-rich ejecta without the degeneracy present in the *Chandra* analysis. The analysis of CCD spectra can be misleading in the estimation of Fe mass by up to a factor of 20. This comparison further confirms that in order to correctly evaluate the ejecta mass it is crucial to

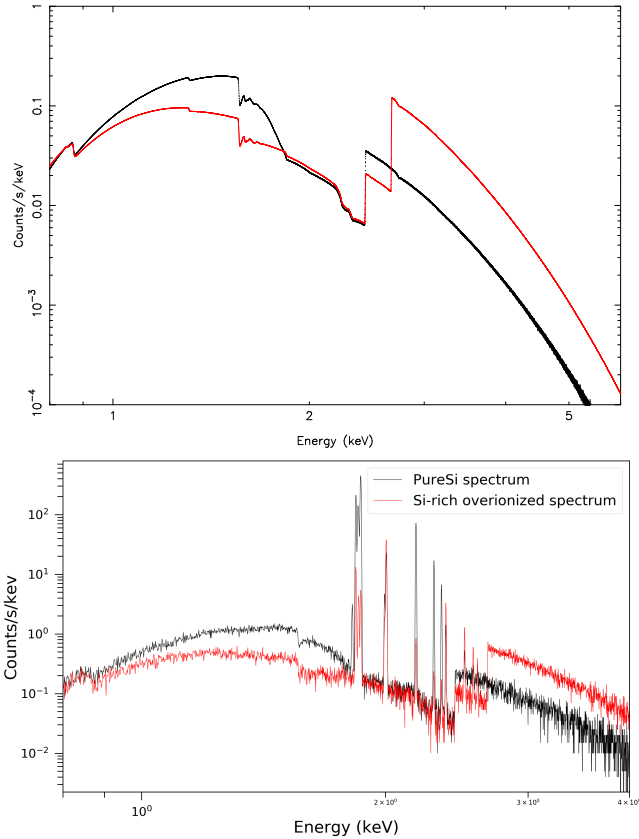


Fig. 10. Comparison between spectra produced by a pure-metal plasma and an overionized plasma. *Upper panel:* in red, continuum-only spectrum of a typical overionized SNR (Si abundance set to 3, $\tau_{\text{rec}} = 10^{11}$ s cm^{-3} , $kT_{\text{fin}} = 0.5$ keV and $kT_0 = 5$ keV); in black, continuum-only spectrum of a typical pure-ejecta plasma in CIE (Si abundance set to 300 and $kT = 0.5$ keV). Both spectra are synthesized assuming an exposure time of 10^8 ks. *Lower panel:* same as upper panel but assuming an exposure time of 100 ks and also including the line emission.

accurately study the RRC of the elements, and high-resolution spectrometers are needed. This is critical since the element mass is used in comparisons with theoretical nucleosynthesis yields.

Acknowledgements. We thank S. Ustamujic and A. Petralia for helpful advice in the development of spectral synthesis tools and J. Mao for help in the use of SPEX software. P.Z. acknowledges support from the NWO Veni Fellowship, grant no. 639.041.647 and NSFC grants 11503008 and 11590781.

References

Arnaud, K. A. 1996, *ASP Conf. Ser.*, 101, 17
Bocchino, F., Maggio, A., & Sciortino, S. 1999, *A&A*, 342, 839

DeLaney, T., Rudnick, L., Stage, M. D., et al. 2010, *ApJ*, 725, 2038
Frank, K. A., Burrows, D. N., & Park, S. 2015, *ApJ*, 810, 113
Gothelf, E. V., Koralesky, B., Rudnick, L., et al. 2001, *ApJ*, 552, L39
Greco, E., Miceli, M., Orlando, S., et al. 2018, *A&A*, 615, A157
Helder, E. A., & Vink, J. 2008, *ApJ*, 686, 1094
Hughes, J. P., Rakowski, C. E., Burrows, D. N., & Slane, P. O. 2000, *ApJ*, 528, L109
Hwang, U., & Laming, J. M. 2003, *ApJ*, 597, 362
Hwang, U., & Laming, J. M. 2012, *ApJ*, 746, 130
Hwang, U., Laming, J. M., Badenes, C., et al. 2004, *ApJ*, 615, L117
Kaastra, J. S., & Jansen, F. A. 1993, *A&AS*, 97, 873
Kaastra, J. S., Mewe, R., & Nieuwenhuijzen, H. 1996, in *UV and X-ray Spectroscopy of Astrophysical and Laboratory Plasmas*, eds. K. Yamashita, & T. Watanabe (Cambridge: Cambridge University Press), 411
Krause, O., Birkmann, S. M., Usuda, T., et al. 2008, *Science*, 320, 1195
Kumar, H. S., Safi-Harb, S., & Gonzalez, M. E. 2012, *ApJ*, 754, 96
Lee, J.-J., Park, S., Hughes, J. P., & Slane, P. O. 2014, *ApJ*, 789, 7
Lide, D. 2003, *CRC Handbook of Chemistry and Physics*, 84th edn. (Boca Raton: Taylor & Francis)
Liedahl, D. A. 1999, *The X-Ray Spectral Properties of Photoionized Plasma and Transient Plasmas*, eds. J. van Paradijs, & J. A. M. Bleeker, *Lect. Notes Phys.* (Berlin: Springer), 520, 189
Lodders, K., Palme, H., & Gail, H. P. 2009, *Landolt Boumlrstein*, 4B, 712
Lopez, L. A., Pearson, S., Ramirez-Ruiz, E., et al. 2013, *ApJ*, 777, 145
Lopez, L. A., Castro, D., Slane, P. O., Ramirez-Ruiz, E., & Badenes, C. 2014, *ApJ*, 788, 5
Matsumura, H., Tanaka, T., Uchida, H., Okon, H., & Tsuru, T. G. 2017, *ApJ*, 851, 73
Mewe, R. 1999, *Atomic Physics of Hot Plasmas*, eds. J. van Paradijs, & J. A. M. Bleeker, *Lect. Notes Phys.* (Berlin: Springer), 520, 109
Miceli, M., Decourchelle, A., Ballet, J., et al. 2006, *A&A*, 453, 567
Miceli, M., Bocchino, F., & Reale, F. 2008, *ApJ*, 676, 1064
Miceli, M., Bocchino, F., Decourchelle, A., Ballet, J., & Reale, F. 2010, *A&A*, 514, L2
Milisavljevic, D., & Fesen, R. A. 2013, *ApJ*, 772, 134
Nakamura, T., Umeda, H., Nomoto, K., Thielemann, F.-K., & Burrows, A. 1999, *ApJ*, 517, 193
Nomoto, K., Hashimoto, M., Tsujimoto, T., et al. 1997, *Nucl. Phys. A*, 616, 79
Okon, H., Tanaka, T., Uchida, H., et al. 2020, *ApJ*, 890, 62
Orlando, S., Miceli, M., Pumo, M. L., & Bocchino, F. 2016, *ApJ*, 822, 22
Ozawa, M., Koyama, K., Yamaguchi, H., Masai, K., & Tamagawa, T. 2009, *ApJ*, 706, L71
Reed, J. E., Hester, J. J., Fabian, A. C., & Winkler, P. F. 1995, *ApJ*, 440, 706
Sawada, M., & Koyama, K. 2012, *PASJ*, 64, 81
Sukhbold, T., Ertl, T., Woosley, S. E., Brown, J. M., & Janka, H.-T. 2016, *ApJ*, 821, 38
Thielemann, F.-K., Nomoto, K., & Hashimoto, M.-A. 1996, *ApJ*, 460, 408
Thorstensen, J. R., Fesen, R. A., & van den Bergh, S. 2001, *AJ*, 122, 297
Uchida, H., Koyama, K., Yamaguchi, H., et al. 2012, *PASJ*, 64, 141
Vink, J., & Laming, J. M. 2003, *ApJ*, 584, 758
Vink, J., Kaastra, J. S., & Bleeker, J. A. M. 1996, *A&A*, 307, L41
Willingale, R., Bleeker, J. A. M., van der Heyden, K. J., Kaastra, J. S., & Vink, J. 2002, *A&A*, 381, 1039
Woosley, S. E., & Weaver, T. A. 1995, *ApJS*, 101, 181
Yamaguchi, H., Ozawa, M., Koyama, K., et al. 2009, *ApJ*, 705, L6
Zhou, P., & Vink, J. 2018, *A&A*, 615, A150
Zhou, X., Miceli, M., Bocchino, F., Orlando, S., & Chen, Y. 2011, *MNRAS*, 415, 244
Zhou, P., Vink, J., Safi-Harb, S., & Miceli, M. 2019, *A&A*, 629, A51

Appendix A: Spectral simulations for the Fe case

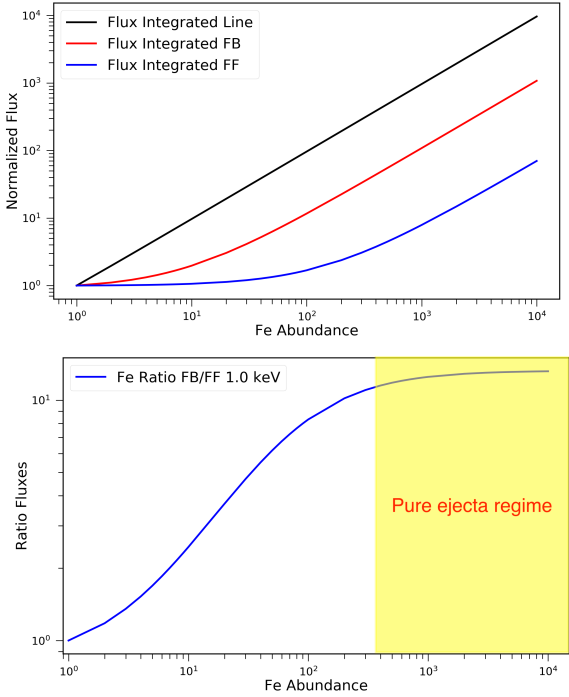


Fig. A.1. X-ray fluxes of different emission processes in the corresponding energy bands (see Table 2) as a function of Fe abundance. *Upper panel:* same as Fig. 1 with Fe instead of Si. *Lower panel:* ratio between the FF and FB fluxes shown in the *upper panel* as a function of Fe abundance for a plasma temperature of 1 keV.

In this section we show the results of the spectral simulations described in Sect. 2.2, by focusing on the Fe abundance. Figure A.1 shows the integrated and normalized fluxes in the corresponding energy bands (see Table 2) of the various emission processes as functions of the Fe abundance, and the corresponding FB over FF ratio. The trend is the same as that already discussed for the Si case with saturation occurring when the Fe abundance is close to one hundred. The study on the temperature dependence of the FB to FF ratio showed that the observability of the Fe RRC is maximized when the electron temperature is in the range 1.5–3.5 keV (see Fig. A.2). We also notice that there are different recombination edges, corresponding to the different Fe ionization states, and that the brightest RRC depends on the temperature and on the degree of ionization of the plasma. In any case, the conclusions obtained for a specific Fe RRC are also valid for the other ones.

For all the syntheses we are going to discuss in this section we consider a distance of 1 kpc and an absorbing column density of $n_H = 5 \times 10^{21} \text{ cm}^{-2}$, unless otherwise stated. We synthesized a pure-Fe spectrum with abundances of all elements except Fe set to 3, Fe abundance set to 300, $kT = 1.5 \text{ keV}$, and a particle density of 3 particles per cm^3 . The resulting spectrum (black crosses in Fig. A.3), synthesized assuming that the emission originates from a clump with radius $R_{\text{clump}} = 1.6 \text{ pc}$, showed the same issues faced with Si synthesis, due to the spectral resolution of the CCD detectors. We here chose a clump larger than that of the Si case because the considered RRC is in a part of the spectrum where the ISM emission is more significant (i.e., the ejecta FB emission is less visible). In any case, we verified that the goodness of our conclusions are not affected by this choice, as we also showed by discussing the realistic case of Cas A in Sect. 4.

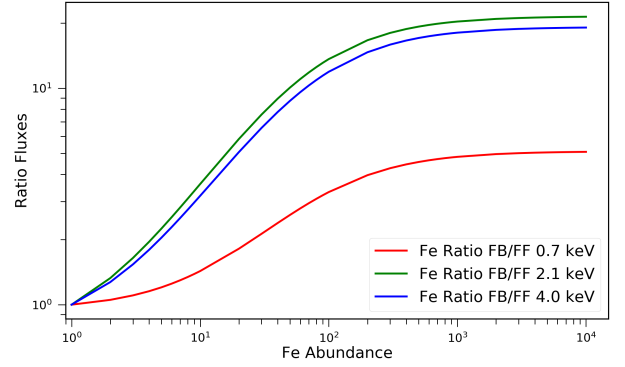


Fig. A.2. Same as lower panel of Fig. A.1 for plasma temperatures of 0.7 keV (red line), 2.1 keV (green), and 4.0 keV (blue).

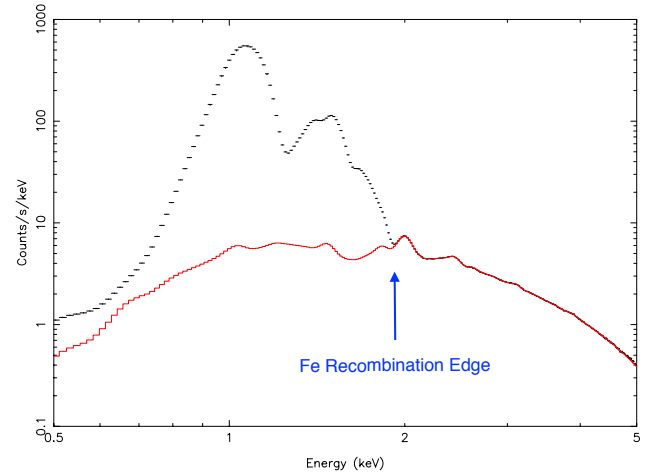


Fig. A.3. Synthetic ACIS-S spectra with high Fe abundance. Black: synthetic ACIS-S spectrum of a CIE plasma with abundance of all elements but Fe set to 3, Fe abundance set to 300, $kT = 1.5 \text{ keV}$, and $\text{EM} = 1.5 \times 10^{56} \text{ cm}^{-3}$. Red solid: same spectrum but with the line emission subtracted.

In addition, the scenario is even more complex because of the huge amount of Fe lines (from Fe XIV to Fe XXIV) present at energies around 1 keV. By ignoring the line emission of all the elements, we notice that the effective continuum contribution (red solid line of Fig. A.3) to the emission shows an edge of recombination at the characteristic energy of Fe XXIV RRC.

We then produced synthetic spectra by adding another CIE component related to the ISM emission, considering the same region described in Sect. 3.1 for the Si case. We chose $T_{\text{ISM}} = 0.23 \text{ keV}$ and $T_{\text{clump}} = 1.5 \text{ keV}$. Even though the high temperature chosen for the clump maximizes the FB emission (as discussed above), we here show that CCD spectrometers cannot reveal the recombination edge. The parameters used for this pure-metal model and the derived Fe and total ejecta mass are summarized in Table A.1. The produced spectra, folded with ACIS-S/Chandra and Resolve/XRISM response matrices, are shown in the upper and lower panels of Fig. A.4, respectively.

We also produced a spectrum considering the mild-ejecta scenario (see again Table A.1) in which the Fe abundance is set to 3 (instead of 300) and the ejecta EM is set to $1.5 \times 10^{58} \text{ cm}^{-3}$. This spectrum is shown in both panels of Fig. A.4. The results of the simulations performed on Fe are analogous to the Si ones and confirm that the instrumental broadening of the line completely hides the possible presence of RRC related to the pure-metal ejecta emission.

Table A.1. Parameters of the ISM (CIE) plus pure-Fe (CIE) model used for the spectral synthesis.

Parameter	ISM	Pure-metal	Mild-ejecta
Emission measure (cm^{-3})	1.6×10^{59}	1.5×10^{56}	1.5×10^{58}
Temperature (keV)	0.23	1.5	1.5
Fe abundance	1	300	3
Fe mass (M_{\odot})	/	0.3	0.04
Ejecta mass (M_{\odot})	/	0.6	6

Notes. The abundance of other elements in the ejecta component is set to 0.

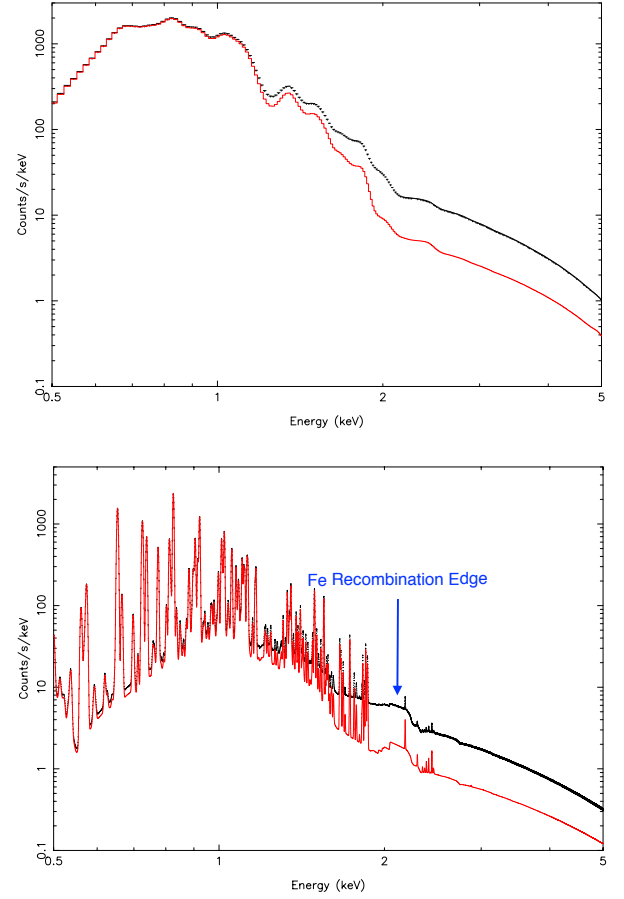


Fig. A.4. ACIS-S and Resolve spectra synthesized from a CIE+CIE model. *Upper panel:* synthetic ACIS-S spectra of ISM+pure-Fe (pure-metal model, red) and ISM+Fe-rich (mild-ejecta model, black) plasmas. *Lower panel:* same as upper panel but the model is folded with the Resolve response matrix.